Thiolate end-group regulates ligand arrangement, hydration and affinity for small compounds in monolayer-protected gold nanoparticles

Thiolate end-group regulates ligand arrangement, hydration and affinity for small compounds in monolayer-protected gold nanoparticles

Elena Pellizzoni,[a,1] Maria Şologan,[a] Mario Daka,[a] Paolo Pengo,[a] Domenico Marson,[b,1] Zbyšek Posel,[b,c] Stefano Franchi,[d,2] Luca Bignardi,[e] Paola Franchi,[f] Marco Lucarini,[f,] Paola Posocco,[b,*] and Lucia Pasquato[a,*]*

[a] Department of Chemical and Pharmaceutical Sciences and INSTM Trieste Research Unit, University of Trieste, 34127 Trieste (Italy)
[b] Department of Engineering and Architecture, University of Trieste, 34127 Trieste (Italy)
[c] Department of Informatics, Jan Evangelista Purkyně University, 400 96 Ústínad Labem (Czech Republic)
[d] Elettra Sincrotrone Trieste S.C.p.A., 34149 Trieste (Italy)
[e] Department of Physics, University of Trieste, 34127 Trieste (Italy)
[f] Department of Chemistry "G. Ciamician", University of Bologna, I-40126 Bologna (Italy)

[1] These authors contributed equally to the work.

[2] Present address: Consiglio Nazionale delle Ricerche - Istituto di Struttura della Materia 00133 Roma – Italy

*Corresponding author
E-mail address: marco.lucarini@unibo.it; paola.posocco@dia.units.it; lpasquato@units.it.

Abstract

The ability to control the properties of monolayer protected gold nanoparticles (MPNPs) discloses unrevealed features stemming from collective properties of the ligands forming the monolayer and presents opportunities to design new materials. To date, the influence of ligand end-group size and capacity to form hydrogen bonds on structure and hydration of small MPNPs (< 5 nm) has been poorly studied. Here, we show that both features determine ligands order, solvent accessibility, capacity to host hydrophobic compounds and interfacial properties of MPNPs. The polarity perceived by a radical probe and its binding constant with the monolayer investigated by electron spin resonance is rationalized by molecular dynamics simulations, which suggest that larger space-filling groups – trimethylammonium, zwitterionic and short polyethylene glycol – favor a radial organization of the thiolates, whereas smaller groups – as sulfonate – promote the formation of bundles. Zwitterionic ligands create a surface network of hydrogen bonds, which affects nanoparticle hydrophobicity and maximize the partition equilibrium constant of the probe. This study discloses the role of the chemistry of the end-group on monolayer features with effects that span from molecular- to nano-scale and opens the door to a shift in the conception of new MPNPs exploiting the end-group as a novel design motif.

Keywords: Nanochemistry, Supramolecular Chemistry, Electron Spin Resonance, Molecular Simulations, MD, Weak Interactions, Hydrophobic Binding.

1. Introduction

The simultaneous control of topology and solvation of functional groups in a catalytic site is achieved in natural systems with proper folding of the proteic polymer.[1] This has significant influence on cell-protein interaction,[2,3] internalization mechanisms,[4,5] recognition[6] and catalytic processes,[7] to mention a few. In an attempt to mimic Nature's "machines" scientists have turned their attention to synthetic models such as micelles[8] or liposomes.[9-13] Metal nanoparticles (NPs) coated by organic monolayers of self-assembling ligands (SAMs) have also been studied as protein-mimicking, catalytic artificial systems by exploiting their inherent multivalence, cooperativity, nanoconfinement, and control achieved in their preparation.[14-16] Indeed, properties of SAM-NPs can be modulated by a variety of parameters[17-22] such as ligand chemistry, functional groups exposed on the surface, nanoparticle dimension, ligand length and density, molecular composition of the monolayer, and ligand organization for heteroligand shells.[23-25] All these parameters impact on the activity of NPs and the way they interact with solvent[26,27] and external (biological) environment.[28-33]

Ligand end group chemistry is a key element able to impart to the nanoparticles specific ability, properties, controlled colloidal stability and dispersibility.[33] Yet, studies aimed to rationalize this effect on monolayer structure and ligand environment are isolated and a general framework lacks. This is particularly relevant for small and ultrasmall NPs – namely below 5 nm – where *i*) the high surface curvature impacts more on ligand arrangement than in larger NPs, which rather resemble 2-D SAM and *ii*) the surface chemistry plays a central role in regulating the transient bionano interactions with proteins and cell membranes.[31,32] The lack of studies on ligand end group effect is partially due to the difficulty in characterizing the monolayer structure. In the solid state information about the organization of the shell is retrieved from X-Ray structure analysis of small gold clusters/nanoparticles,[34-36] protected by ligands designed to impart rigidity to the SAMs and

presenting relatively short alkyl chains and/or aromatic rings. However, this cannot be extended to larger NPs functionalized by flexible and longer thiolates. Thus, probing ligand distribution in solution on larger NPs is still extremely challenging.[37]

As indeed stated by Grzybowski recently, "*we have only an indirect understanding (from simulations) of how the ligand shell is organized*".[33] For instance, Glotzer described the influence of alkanethiolate chain length, temperature and nanoparticle size on ligand arrangement.[38] Below 450 K, molecular dynamics (MD) calculations suggest long-range ordering of thiolates having more than 9 carbon atoms. They form clusters (e.g. bundles), similar to those of alkanethiols on flat Au(111) surfaces, but with larger tilting angles. For longer chain lengths (9 and 17 carbons) Grest[39] reported on the effect of the end group (CH_3, NH_2, COOH) and its ionization state on the structure of gold NPs (AuNPs) coated with ω-functionalized alkylthiolates in water and decane. This analysis was later expanded by Sphor[40] for AuNPs coated with 6 to 24 carbon atom long chains, linear and branched. Both computational studies supported a chain length dependence of the hydrophobic bundling and a negligible influence of the head group chemistry. Repulsion between charged chains seems to mitigate ligand association and favours more disordered conformations.

Coupling indirect experimental approaches with theoretical or computational models has been of help in overcoming such limitations.[41-43] In a recent work by Murphy,[19] the combination of NMR and implicit solvent MD simulations suggests that monolayers of (16-mercaptohexadecyl)trimethylammonium bromide on AuNPs organize in a radial fashion (following the continuous model introduced by Landman[44,45]) with end groups more closely packed in larger than in smaller (< 10 nm) NPs. Nonetheless, the divergent mode of ligand organization – radial vs. bundled – on metal NP surface has not found a rational harmonization in

literature and the definition of which aspects direct ligand ordering toward a specific arrangement has not fully emerged.

Solvation energy contribution to SAM organization needs to be considered, especially when there are polar end groups that strongly interact with the solvent molecules,[41] or charged groups as ammonium ions, carboxylates and sulfonates which may be involved in hydrogen bonds. Moreover, for instance, primary ammonium ions differ from quaternary ones in size, charge density, hydrophilicity and consequently in solvation by water. Additionally, solvent may screen out inter-particle attractive interactions leading to monolayers intergiditation, which in turn is accompanied by a change in the conformational structure of the ligands.[46-48]

Different ligand arrangements mean also different accessibility of solvent and small molecules to the inner of the monolayer. Monolayer accessibility is relevant for sensing[49-53] and drugs binding by weak interactions[54,55] and can be addressed by species sensitive to the polarity of the environment that become good reporters of the hydrophobicity/hydrophilicity of their local surroundings. This is the case of specific radical probes with affinity for the monolayer and whose spectroscopic parameters are influenced by the local environment, thus enabling to gather information about the polarity of the medium by electron spin resonance (ESR) spectra analysis. ESR spectroscopy allows the assessment of the partition equilibrium constant, K_{eq}, of radical probes between monolayer and solvent (**Figure 1**), and the spectroscopic parameters are directly related to the to the hydrophobicity of the medium.[56,57]

In this work, ESR measurements are carried out using the radical probe drawn in **Figure 2**, which has a good affinity for hydrophobic monolayers and whose spectroscopic parameters strictly depend from the local polarity of the surrounding medium and the monolayer.[41,42,49,56-58]

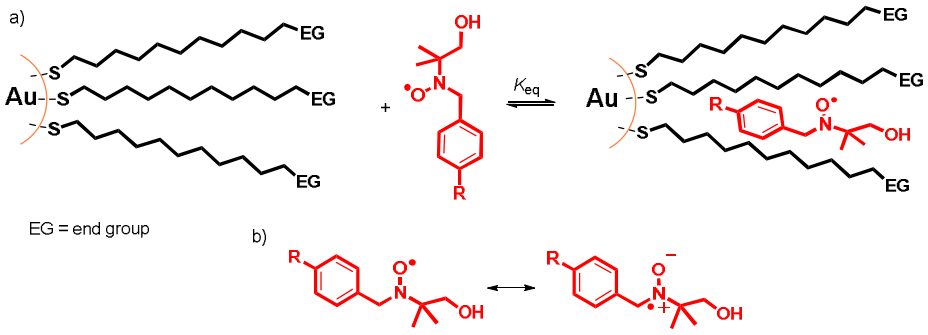

Figure 1. a) Partition equilibrium of a radical probe between water and NP monolayer; b) mesomeric forms of the radical probe: on the left, the one prevalent in hydrophobic media and on the right, that prevalent in hydrophilic media.

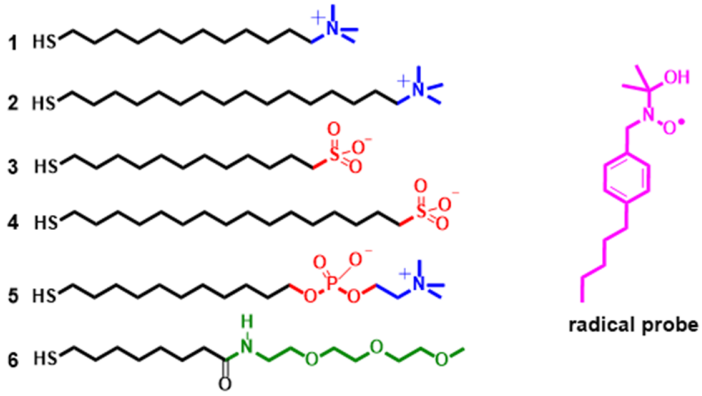

Figure 2. Structure of ligands **1**–**6** used for the preparation of homoligand monolayer-protected AuNPs (**NP1**-**NP6**) and the radical probe used in this study.

ESR spectra, carried out at different temperatures, are analyzed and simulated to determine the hyperfine coupling constants, which are here coupled with MD calculations of NPs to rationalize monolayer structure, solvation, and probe location. ESR measurements at different nanoparticle concentration allow deriving the equilibrium constants of the probe free in solution and within the monolayer, which is an indication of the host properties of the monolayer. Selected NPs are

characterized by synchrotron-based X-ray photoelectron spectroscopy (XPS), in order to estimate the thickness of the self-assembled monolayer and to compare it with data from MD simulations.

We chose ligands, well known in the literature of SAMs, presenting as terminal groups: a positive charged quaternary ammonium ion, ligands **1** and **2,** with alkyl chain of 12 and 16 carbon atoms, respectively, indicated as C12 and C16; a negatively charged sulfonate ion, ligands **3** and **4**, with chains C12 and C16, respectively; a zwitterionic group having an inner phosphate and an ending trimethylammonium group, ligand **5**, and a neutral triethylene glycol monomethyl ether, ligand **6** (**Figure 2**). The thiolates were designed to differ in nature and size of the end-groups as well as in chain length. The gold core diameter, of ~ 4 nm, was selected because of the relevance of the surface chemistry at this size for the interactions with biological entities and was maintained as much as possible constant. In principle, the dimension of NP core (relative to the ligand length) may itself affect the shell organization; lowering the diameter, the chains gain available free volume due to the increased core surface curvature. This reduces the chance of interchain interactions, making ligand clustering more difficult and thus affecting the overall monolayer structure.

The results from this systematic investigation allows us to draw general conclusions on the role of surface group chemistry on ligand arrangement, monolayer hydration and ability to complex small hydrophobic compounds.

2. Materials and methods

Synthesis: Thiols **1**, and **3** were prepared as reported in literature.[59] Detailed procedures for the preparation of thiols **2**, **4**, and **5** and their characterization are described in Supporting Material (SM).

166 The procedure used for the preparation of gold NPs was adapted from ref. 60.[60] The experimental
167 conditions used for the syntheses of **NP1**-**NP5** are the same and in particular the reactions were
168 carried out at room temperature with a ratio between $HAuCl_4$: TOAB : $NaBH_4$ of 1 : 5.4 : 14.5 on
169 a scale of 0.100 g, 0.296 mmol, of $HAuCl_4$ or half of this for **NP3**.
170 *Synthesis of **NP1***: To a solution of tetrachloroauric acid (0.100 g, 0.296 mmol, 1 equiv) in 11.6
171 mL deoxygenated milliQ water, TOAB (0.869 g, 1.59 mmol, 5.4 equiv) in 8.8 mL of deoxygenated
172 chloroform was added and the solution was let to stir for 30 min at room temperature. The two
173 phases were separated and a solution of sodium borohydride (0.161 g, 4.27 mmol, 14.5 equiv) in
174 7.8 mL milliQ water was added to the organic phase and the reaction mixture stirred for 15 minutes
175 under argon atmosphere. After this time a solution of **1** (0.010 g, 0.034 mmol) in 6 mL isopropanol
176 was added and the nanoparticles precipitated. After 1.2 h the solid was separated and the
177 nanoparticles were washed six times with chloroform (6 x 15 mL) (4500 rpm, 4 min, 25 °C). TEM:
178 4.4 ± 1 nm, n = 495. DLS: D_H 7.97 ± 1.98 nm. TGA 15 %. Average composition: $Au_{2950}C12N_{385}$.
179 *Synthesis of **NP2***: A solution of TOAB (0.868 g, 1.59 mmol, 5.4 eq) in 9 mL of chloroform was
180 added under argon atmosphere to an aqueous solution of tetrachloroauric acid (0.100 g, 0.296
181 mmol, 1 eq) in 11.6 mL milliQ water at 25 °C and the reaction was let to stir for 15 minutes. The
182 two phases were separated and a solution of sodium borohydride (0.161 g, 4.27 mmol, 14.5 eq) in
183 7.8 mL of water was added to the organic phase. The red colored solution was stirred for 15
184 minutes and then a solution of **2** (0.015 g, 0.042 mmol) in 8.2 mL of isopropanol was added. Under
185 these conditions the nanoparticles precipitated and the dispersion was stirred for 2 hours. The solid
186 was separated and washed with chloroform (5 x 30 mL, 4500 rpm, 5 min). TEM: 4.2 ± 0.9 nm (n
187 = 307). DLS: D_H 7.66 ± 2.10 nm. TGA 16%. Average composition: $Au_{2759}C16N_{326}$.

*Synthesis of **NP3***: $HAuCl_4 \cdot xH_2O$ (0.050 g, 0.147 mmol, 1 eq) was dissolved in 5.8 mL of deoxygenated water and stirred for 30 min at room temperature with a solution of TOABr (0.435 mg, 0.795 mmol, 5.4 eq) in 4.4 mL of deoxygenated chloroform. The colorless aqueous layer was discarded, while the orange organic phase containing the gold ions was placed in a round bottomed flask and, under vigorous stirring, a cold solution of $NaBH_4$ (0.081 mg, 2.133 mmol, 14.5 eq) in deoxygenated water (3.9 mL) was quickly added. After stirring for 15 min at room temperature, a dark red-violet dispersion of nanoparticles in chloroform was obtained. The aqueous phase was discarded and the organic solution was divided equally in two flasks.

To the first sample a solution of thiol **3** (0.007 g, 0.025 mmol) in 3.3 mL of 2:1:0.3 deoxygenated methanol:isopropanol:DMF was added dropwise to the nanoparticles solution in chloroform. The suspension was stirred for 1.20 h at r.t. After wash with chloroform (4 x 20 mL) and ethanol (3 x 20 mL) and centrifugation at 4200 rpm for 5 min, nanoparticles were dried under flux of argon and characterized. Nanoparticles are soluble in water. TEM: 4.1 ± 1.0 nm, n = 557. DLS: D_H 6.69 ± 2.05 nm. TGA: 15,3%. Average composition: $Au_{2600}MDDS_{330}$.

*Synthesis of **NP4***: $HAuCl_4 \cdot xH_2O$ (0.100 g, 0.294 mmol, 1 eq) was dissolved in 11.6 mL of deoxygenated water and stirred for 30 min at 25 °C with a solution of TOAB (0.869 g, 1.59 mmol, 5.4 eq) in 8.8 mL of deoxygenated chloroform.

After the colorless aqueous layer was discarded and a cold solution of $NaBH_4$ (0.161 mg, 4.27 mmol, 14.5 eq) in 7.8 mL deoxygenated water was quickly added to the orange organic phase containing gold and the mixture was vigorously stirred for 15 min at 25°C. Finally, the aqueous layer was removed and a dark red-violet solution of nanoparticles in chloroform was obtained. 0.013 g (0.036 mmol) of thiol **4** were dissolved in 8 mL of deoxygenated 3:1 methanol:isopropanol mixture, and the obtained solution was added dropwise to the nanoparticles solution. After stirring

for 1.20 h at 25 °C, precipitated nanoparticles were washed by centrifugation with chloroform pretreated with K_2CO_3 (5 x 20 mL) and methanol (5 x 20 mL). The obtained nanoparticles were characterized by ^{1}H-NMR spectroscopy, TEM and UV-vis spectroscopy. The obtained nanoparticles are soluble in water with 10% of isopropanol. TEM: 4.4 ± 1.0 nm, n = 550. DLS: D_H 14.86 ± 4.25 nm. TGA 16%. Average composition: $Au_{2950}MHDS_{384}$.

*Synthesis of **NP5***: A solution of TOAB (0.084 g, 5.4 eq) in chloroform (7.6 mL) was added, under argon atmosphere, to an aqueous solution of tetrachloroauric acid (0.084 g, 0.247 mmol, 1 eq) in 10 mL of deoxygenated milliQ water, at 25 ºC and the reaction was let to stir for 15 minutes. The two phases were separated and a solution of sodium borohydride (0.135 g, 3.58 mmol, 14.5 eq) in 11.5 mL of water was added to the organic phase. The red colored solution was stirred for 15 minutes and then a solution of thiol **5** (0.016 mg, 0.042 mmol) in 6.9 mL isopropanol was added. The nanoparticles precipitated and the dispersion was stirred for 2 hours. The precipitate was separated and washed five times with chloroform (30 mL, 4500 rpm, 5 min). TEM: 4.4 ± 0.9 nm, n = 313. DLS: D_H 6.30 ± 0.92 nm. TGA: 18%. Average composition: $Au_{3000}ZW\text{-}PN_{360}$.

Computational methods: Preparation and simulation of each nanoparticle model followed the protocol described in our previous work[52] and reported here in brief. Ligand **1**-**6** were prepared using antechamber and assigning gaff2 atom types;[61,62] force field parameters for the radical probe were taken from the works of Barone et al.[63,64]. Partial charges were calculated applying the RESP method provided by RED[65] server. Au-Au interactions were described with the parameters of INTERFACE[66] force field for metals. Icosahedral gold cores were built matching the experimental values and the proper number of ligands was then assigned for the functionalization. A harmonic bond was created between each sulfur atom and a gold atom within 3.3 Å with a spring constant 50.000 kJ/mol*nm^2.[67] Although this interface structure disregards possible gold−sulfur

binding motifs, it has been shown recently[67] that this simplified treatment yields a description of the structure of self-assembled alkanethiols of various length (n = 3-15) on 2-6 nm size gold core in agreement with experiments. The systems were then solvated with TIP3P water molecules, extending at least 15 Å from each solute atom, and counterions added to neutralize the system. A combination of steepest descent (10000 cycles) and conjugate gradient (10000 cycles), followed by a heating phase of 100 ps in NVT ensemble (integration step = 1 fs), was carried out to reach the production temperature of 300 K. Then, density was brought to its final value with at least 50 ns in NPT conditions (integration step = 2 fs, pressure 1 atm), and pressure was maintained by Berendsen barostat. Finally, we switched to Monte Carlo barostat for production run, of which the first part was discarded until steady-state of ligands RMSD was reached. Trajectory for final ensemble averages (400 ns) was stored from this point on. Temperature was controlled by Langevin method (damping coefficient of 5 ps^{-1}) throughout all simulations. Electrostatic interactions were computed by means of Particle Mesh Ewald (PME) algorithm, and calculations were carried out using AMBER 18.[68-71] Analysis was conducting using AMBERTools18 and in-house Python scripts. Results were ensemble averaged on three repeated calculations. For systems containing the probe, the radical was placed close to the equilibrated monolayer (not in contact) changing initial position and orientation of the probe with respect to the NP and assigning different starting velocities to enhance the sampling of the binding for a total of 1.6 μs time of simulation. Further details are provided in the SM.

3. Results and discussion

3.1. Ligand packing is sensitive to the size and hydrogen bonding capability of the end-group

The ESR spectra of the radical probe were characterized by two resolved set of signals, see for **NP1 Figure 3** as an example. The one with larger hyperfine coupling constants is due to the radical

located in water, while the second one arises from the radical hosted in the less polar environment of the monolayer, in equilibrium with the free nitroxide (see **Figure 1**), and has a nitrogen hyperfine splitting (a_N, see **Table 1**) significantly smaller than that measured for the radical in solution.

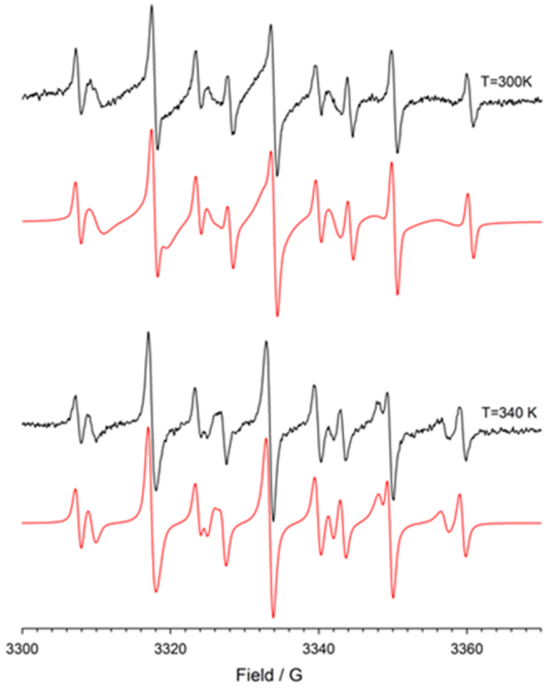

Figure 3. ESR spectra of the radical probe recorded in the presence of **NP1** (13.5 mg/0.1 mL) at 300 K (top) and 340 K (bottom) in water. In red are reported the corresponding theoretical simulations, NRMSD (normalized root mean square displacement, RMSE/data range) 0.024 at 300 K and 0.028 at 340 K.

Table 1. Spectroscopic parameters for the radical probe and partition equilibrium (K_{eq}) constants.

NP	T (K)	a_N (G)	a_{2H} (G)	K_{eq} (M^{-1})
-	300	16.25	10.14	
-	340	16.22	9.80	
NP1	300	15.20	8.50	131
NP1	340	15.34	8.46	30
NP2	300	**14.50**[a]	**8.45**[a]	
NP2	300	15.18[b]	8.58[b]	
NP2	340	15.15	8.50	320
NP3	300	15.15	8.40	133

NP3	340	15.40	8.48	26
NP4	300	**14.40**[a]	**8.38**[a]	
NP4	300	15.23[b]	8.30[b]	
NP4	330	**14.58**[a]	**8.40**[a]	
NP4	330	15.33[b]	8.33[b]	
NP4	340	15.32	8.40	98
NP5	300	15.25	8.35	550
NP6[c]	298	15.70	9.00	77

[a)] The values given in bold type refer to probe in the most hydrophobic location. [b)] These values refer to the less hydrophobic location of the probe. [c)] Data from ref. [56].

The spectroscopic parameters of the radical in the monolayer were very similar for **NP1**, **NP3** and **NP5** with a_N in the range of 15.15 – 15.25 G (**Table 1**), suggesting that the probe is experiencing a similar polarity even in presence of differently charged end groups. Surprisingly, these a_N values are 0.55 – 0.45 G units smaller than the corresponding value measured in previous works, when the same radical probe is immersed in the monolayer of ligand **6** (**NP6**, a_N = 15.7 G),[56] and even smaller than those measured in fluorinated monolayers.[58] This observation reflects a higher hydrophobicity experienced by the probe in the monolayer of **NP1**, **NP3** and **NP5** compared to **NP6**. Such behaviour was unexpected especially for **NP3** and **NP5**, where the probe hydroxyl moiety could, in principle, form hydrogen bonds with the oxygen atoms of sulfonate groups in **NP3** or with the oxygen of phosphate groups in **NP5**, thus bringing the nitroxide moiety of the probe more exposed to the aqueous medium and leading to an a_N value close to that measured for **NP6**.

At molecular level, MD calculations showed that in **NP6** ligands organize radially around the core (**Figure 4**), stabilized by the presence of interchain and chain/water hydrogen bonds (**Figure S1a** and **Table S1**). This is consistent with the disordered bent conformation of the PEG-end group and the presence of interligand C=O···H-N hydrogen bonds as suggested by Rotello on the basis of IR measurements[72] and more recently by Mancin and De Vivo,[73,74] which also provide a degree of asphericity to the monolayer (**Table S2**). In agreement with the ESR data, the radical

probe is completely immersed within the monolayer and oriented with the polar head in the hydrophilic outer layer and the *para*-alkyl tail in the hydrophobic inner region (**Figure S2a**). Radial distribution function (RDF) of the nitrogen atom of the probe allowed determining its average position, which is centered at 1.28 nm (*N*-peak) distant from the gold surface, where it is surrounded by a relatively hydrated environment (**Figure S2b** and **c**).

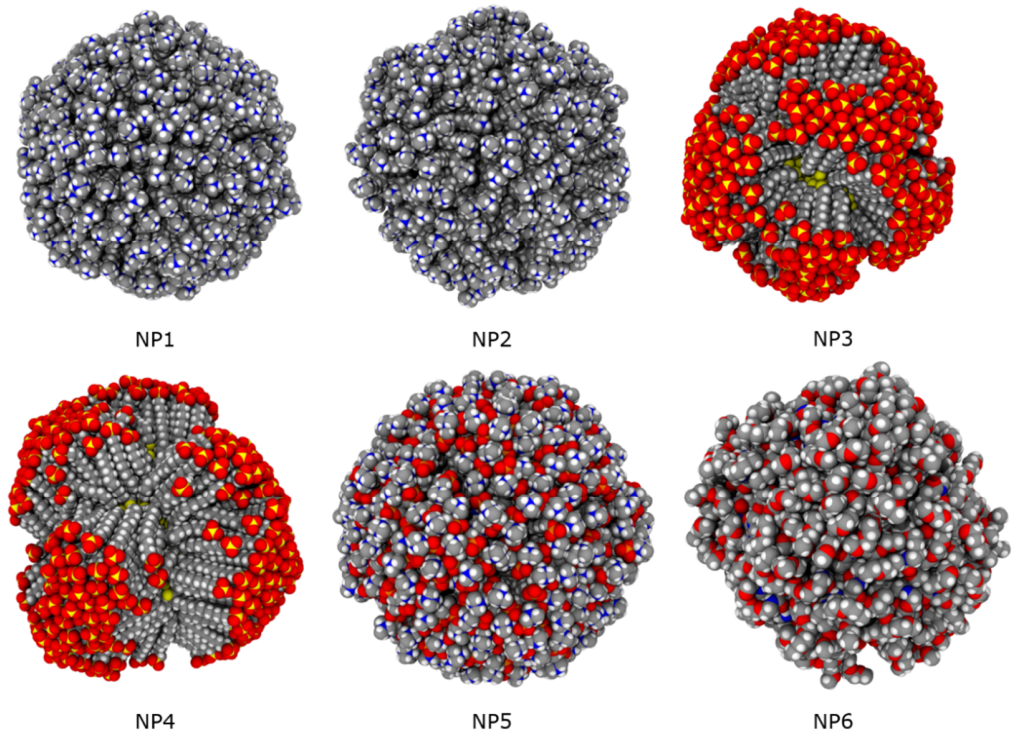

Figure 4. Space-filling model of monolayer organization around the NP gold core as obtained from MD calculations for **NP1**-**NP6**. Solvent is not shown for clarity. Color legend: carbon, grey; oxygen, red; sulfur, yellow; phosphorous, orange; nitrogen, blue; hydrogen, white.

By contrast, at 300 K, when **NP1** and **NP3** are considered, the nitrogen atom of the probe is located at 1.46 and 1.34 nm (**Figure S3**), respectively, from the surface with its axis almost perpendicular to the ligands axis (**Figure 5**). While **NP1** shows an isotropic distribution of ligands around the core and a spherical shape, chains in **NP3** associate in more elongated bundles with almost all

chains in *trans* conformation (**Figure 4** and **Table S2**); thus, it appears that the sulfonate end-group with its less bulky nature allows ligands to better compact and order themselves establishing favourable interchain interactions. At the same time, ligands may be kept close by forming water bridges and hydrogen bonds with water molecules, which relief the electrostatic repulsion between the sulfonate groups (**Table S1** and **Figure S1b**).

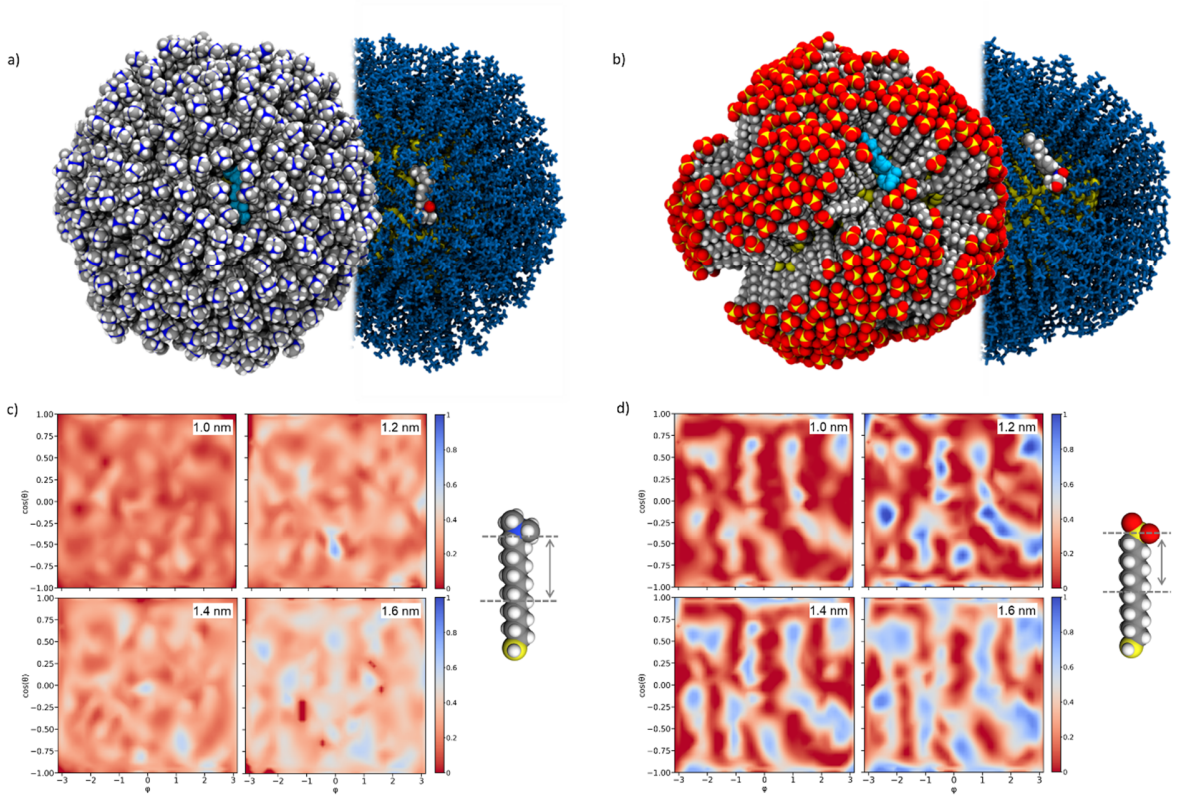

Figure 5. Binding of the radical probe within **NP1** (a, left) and **NP3** (b, left) in space-filling model. Solvent is not shown for clarity. Color code: probe, cyan; carbon, grey; oxygen, red; sulfur, yellow; nitrogen, blue; hydrogen, white. The probe is colored by atomic element (carbon, grey; nitrogen, blue; oxygen, red; hydrogen, white) in each right side of panel a/b, and the monolayer is depicted as blue sticks. Normalized water distribution at increasing distance from the gold surface for **NP1** (c) and **NP3** (d). The graphs plot the distribution of the atom (oxygen of water or carbon of thiolates) closest to gold surface (centered on the gold core and placed at increasing distances from its surface) shown as a two-dimensional projection of the sphere surface (x-axis, the azimuthal angle φ; y-axis, the cosine of the polar angle θ). Value of 1 indicates that an oxygen atom of a water molecule is always the closest; if it is equal to 0, it indicates that a carbon atom of a chain is always the closest. Simplifying, red to salmon areas represent poorly hydrated zones, while blue areas stand for highly hydrated parts of the monolayer (at a certain distance from the gold surface). At distances lower than those considered the microenvironment is almost hydrophobic, while at

higher distances it is fully hydrated and no major difference between the monolayers could be then detected. For bundled monolayer morphologies as in **NP3**, red areas are mainly constituted by space points belonging to ligand bundles. The arrow superimposed to ligand **1** (c) and **3** (d) structure helps to identify visually the region within the monolayer which the water maps refer to.

Despite thiols **1** and **3** have a comparable hydrophobic portion, the presence of a bulky end-group and steric hindrance effect, in the former, forces the monolayer to adopt a radial organization. Consequently, the probe is located isotropically inside the shell in the monolayer of **NP1** (**Figure 5a**), whereas in **NP3** it binds the monolayer at bundle interface, deep in the valley between bundles (**Figure 5b**).

Interestingly, regardless the different monolayer organization and interaction position, the probe shares in **NP1** and **NP3** a similar hydration environment as identified from water density distribution at radial distances close to the average nitrogen position of the probe (compare **Figure 5c** and **5d**). This provides a molecular interpretation of the similarity in the spectroscopic parameters $a_N(G)$, $a_{2H}(G)$ found in the ESR measurements. Furthermore, the averaged hydration values around the nitrogen atom of the probe in **NP1** or **NP3** are much lower compared to that in **NP6**, supporting higher hydrophobicity of these two monolayers compared to monolayer of ligand **6** in agreement with ESR data in **Table 1**.

For **NP5** MD simulations predicted a radial organization of the chains (**Figure 4**) and the nanoparticle adopts a spherical shape with a slightly lower fraction of *trans* dihedrals respect to **NP1** (**Table S2**). The thickness of the self-assembled monolayer, obtained from XPS data according to the methodology described by Shard,[75] is of 1.37 nm (see SM for further details on the methodology), in good agreement with the computational average value of 1.58 nm, supporting the folding at the phosphate group, which exposes both ions to water. Also in this case, the presence of bulky end groups hinders ligand association in long-living bundles. The radial conformation is

stabilized by a significant amount of hydrogen bonds, both involving ligand-water and ligand-water-ligand interactions (**Table S1** and **Figure S1c**)). This induces a stable hydration network in the outer layer of the shell, and hampers further solvent penetration as it can be clearly assessed by comparing solvent density distributions for **NP5** and **NP1** systems (**Figure S4c** and **5c**). At the same distance from the gold core, the monolayer of **NP5** appears much less hydrated than **NP1**. The probe is mainly placed 1.55 nm far from the gold surface (**Figure S4b**), where the average water distribution is comparable to that observed close to the *N*-peak in **NP1** and **NP3**, thus explaining the similarity of the spectroscopic parameters for these systems.

As expected, hydrogen bond formation between the probe and the oxygen atoms of the phosphate is detected; however, these bonds exist only for 67% of the simulation time, which is lower than the 80% calculated for **NP6** (**Figure S5**). Taken together, these evidences justify the unexpected lower value of a_N of **NP5** compared to **NP6**.

3.2 The probe is hosted in a complex environment in thicker monolayers and binding is maximized by zwitterionic end-groups

A different behaviour was instead observed in presence of monolayers composed of longer hydrocarbon chains containing 16 carbon atoms, i.e. **NP2** and **NP4**. **Figure 6a** shows the ESR spectrum of the nitroxide probe recorded at 300 K in the presence of **NP4**. The spectrum of the radical probe is characterized by the presence of two set of signals due to the radical hosted in the less polar environment of AuNP monolayer, in equilibrium with the free nitroxide.

However, comparison of the values of a_N for the radical located in the longer **NP4** and shorter **NP3** monolayer indicates that it is substantially smaller (in Gauss equal to –0.70) in the former case (**Table 1**). This suggests that the probe in **NP4** is positioned in an environment having a

polarity lower than that experienced in the shorter chain monolayer of **NP3,** hereafter named **probe@position1**.

By increasing the temperature, a new set of signals, characterized by spectroscopic parameters very similar to those previously measured in the monolayer of **NP3** appears in the spectrum, named **probe@position2** (**Figure 6a**, 330 K, and **Table 1**). The presence of this new triplet of triplets is indicative of two diverse sites where the radical is located in the monolayer experimenting different polarities.

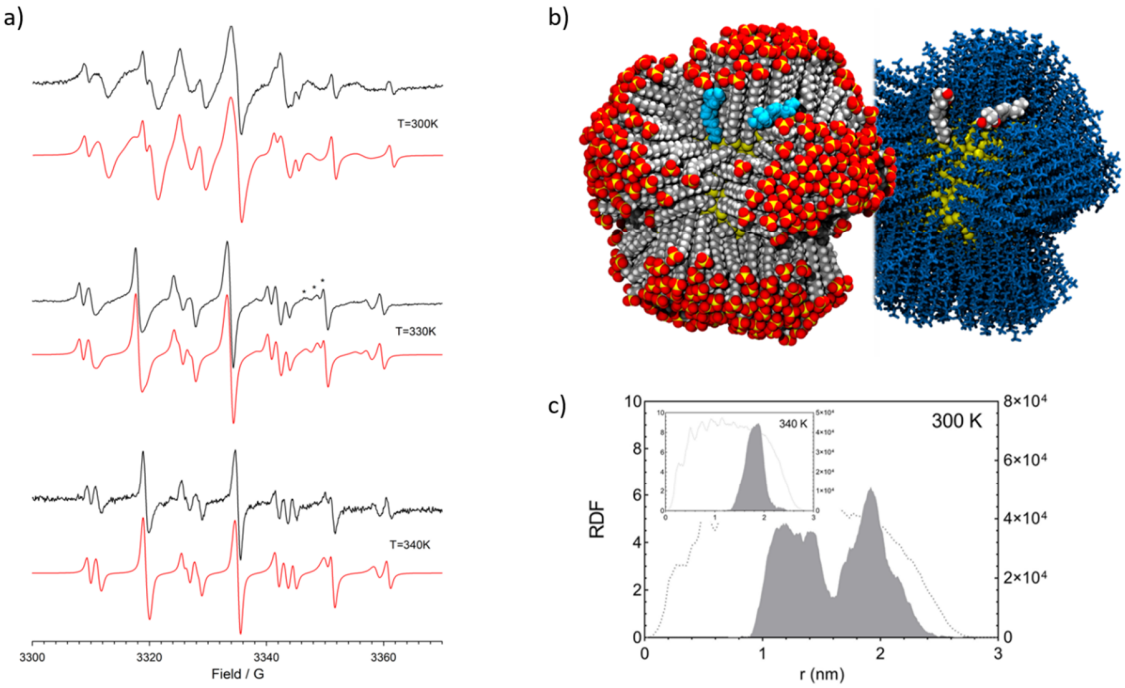

Figure 6. a) ESR spectra of the radical probe recorded in the presence of **NP4** (13.3 mg/0.1mL) at 300 K (top), 330 K (middle) and 340 K (bottom). Stars refer to the three different radical species (see text). In red are reported the corresponding theoretical simulations; NRMSD: 0.035 at 300 K, 0.0164 at 330 K and 0.044 at 340 K. b) Representative binding mode of the radical probe within **NP4 @position1** and **@position2** from MD simulations at 300 K in space-filling model. Color code: probe, cyan; carbon, grey; oxygen, red; sulfur, yellow; hydrogen, white. Positions are superimposed to allow visual comparison. The probe is also reported by atomic element (carbon, grey; nitrogen, blue; oxygen, red; hydrogen, white) in the right side of panel (b), and the monolayer

is depicted as blue sticks. c) MD radial distribution function (RDF) of nitrogen atom of the radical probe in the monolayer of **NP4** at 300 K (solid line, left axis) and ligand **4** (dotted line, right axis) reported from the gold surface. Inset: same RDFs as in panel c), but predicted at 340 K.

The relative concentration of the probe in these two positions changes reversibly varying the temperature, being **probe@position2** the dominant species at higher temperatures (340 K, **Figure 6a**). Thus, we were able to reproduce the experimental spectra by considering different amount of the radical specie located in the three different environments at different temperatures in the corresponding theoretical simulations (see red line in **Figure 6a**). The quantitative determination of the relative amounts of the radical in the different positions, however, was drastically hampered by the poor spectral resolution and only a crude estimation of [***probe@position1***]/[***probe@position2***] ratio was possible. On this basis, we estimated a [***probe@position1***]/[***probe@position2***] ratio equal to ≈ 0.3 and ≈ 2.7 at 300 and 330 K, respectively. Van't-Hoff plot of these data (**Figure S6**), gives rise to approximate thermodynamic parameters ΔH = +13 ± 4 kJ/mol, ΔS = +42 ± 12 $Jmol^{-1}$ K^{-1}, indicating an entropy driven equilibrium for the formation of the ***probe@postion2*** at higher temperatures.

At molecular level, the long ligand **4** assembled into five bundles, which endow the NP with a less rounded structure (**Figure 4** and **Table S2**); as also seen in **NP3**, ligand-water-ligand hydrogen bonds take place between the oxygen atoms of the sulfonate end group, contributing to chain compaction and ligand ordering (**Table S1** and **S2**). The radical probe interacts with **NP4** shell at the energetically-favoured interface between the bundles (**Figure 6b**) and at 300 K the *N*-peak is found at two main distinct locations in contact with the monolayer (**Figure 6c**): the first at 1.26 nm and the second at 1.90 nm from the gold surface, in agreement with experimental ESR data. These positions are characterized by a significantly different hydration. As shown in **Figure S7**,

412 at a distance of 1.26 nm from the core, a limited number of water molecules access the monolayer
413 and the environment is virtually hydrophobic, this corresponding to the **probe@position1** detected
414 by ESR. Moving to 1.90 nm, the probe enters a much more hydrophilic local environment. At
415 higher temperatures (340 K), the two peaks merge in one single peak with an average *N* position
416 at 1.83 nm from the metal surface (**Figure 6c**, inset), which resembles **probe@position2**.
417 Similar experimental results were also obtained with **NP2**. In this case, however, the spectral
418 resolution and the differences in the value of hyperfine splitting constants did not permit to
419 spectroscopically resolve the signals of the radicals partitioned in the two different monolayer
420 environments. It is interesting to note that the larger affinity of the probe for **NP2** monolayer
421 allowed us to record spectra containing mainly the signal due to ***probe@position1*** at 300 K and
422 ***probe@position2*** at 340 K (see **Figure S8**).
423 MD simulations show that despite **NP2** exhibits a uniform radial organization of ligands around
424 the core (**Figure 4**) thanks to the large trimethylammonium end group, two distinct probe locations
425 were found at 300 K (**Figure S9a**); the first, with the *N*-peak at 1.02 nm from Au surface and
426 poorly hydrated, corresponds to the low-polarity **probe@position1**. The second, placed at 1.64
427 nm, is more hydrated and well describes **probe@position2** (**Figure S9b**). The peaks merge in one
428 single peak at 340 K (1.83 nm) (**Figure S9a**). XPS data acquired on **NP2** support these outcomes,
429 returning a thickness of the organic shell around the metal core of ca. 1.88 ± 0.10 nm (see SM)
430 indicative of a fully extended alkyl chain, which agrees well with the high percentage of *trans*
431 dihedrals in the ligand chains (**Table S2**).
432 Thus, sufficiently long ligand chains allow the probe to bind in two distinct sites, not observed
433 in monolayers composed of shorter ligands, one located deeper in the shell and the other more
434 exposed to the exterior.

Relevant is the analysis of K_{eq} values measured by ESR (**Table 1**), which is also consistent with the monolayer packing picture offered by MD simulations. In general, the partition equilibrium constants are lower at higher temperature as expected from the thermodynamics of the process and increase with the thickness of the hydrophobic portion of the monolayer up to one order of magnitude, see data for **NP1** vs. **NP2** and **NP3** vs. **NP4** in **Table 1**. Moreover, the presence of open canyons allows easier ingoing and outgoing of the probe compared to radial monolayers, and is consistent with the lower K_{eq} measured for **NP4** with respect to **NP2**. Additionally, the zwitterionic monolayer in **NP5** favours the complex formation by a factor of 4 with respect to **NP1** and **NP3**, presenting the same hydrophobic monolayer thickness.

4. Conclusions

Experimental ESR studies combined with MD simulations suggest that the packing mode of self-assembled monolayers on gold nanoparticles with a core of ~ 4 nm is affected by the nature and space occupied by ligand end group. Larger size surface groups such as trimethylammonium, zwitterionic and PEG groups, lead to a radial organization and the end-group contribution overcomes association-promoting interactions, as van der Waals and solvophobic forces. On the contrary, smaller end-groups, such as sulfonate ones, allow chains to arrange closer and establish further stabilizing interactions (such as hydrogen bonds), which cooperate to make ligand bundles long-living. This has significant consequences on hydration of the monolayer, local environment and solvent distribution within the shell, which is more uniform in radially organized than anisotropic monolayers.

Another key finding is that for long enough chains two positions at distinct polarity exist, where a hydrophobic host could be detected, opening to the design of monolayers able to promote

458 catalytic events influenced by the number of water molecules present in the catalytic site, similarly
459 to enzymes.
460 Thus, the role of the end-group is not limited to the surface properties but its nature influences
461 structure and hydration of the whole self-assembled monolayer. This study reveals that one,
462 simple, molecular-level parameter (chemical nature and size of NP surface group) affects the
463 monolayer properties across several length scales, from molecular- up to nano-scale.
464 We trust that this work will offer novel perspectives on the molecular features controlling the
465 behaviour of SAM protected gold nanoparticles, their ability to host hydrophobic drugs and
466 interface with exogenous molecules as nanocarriers or nanoreceptors with tailored affinity and
467 selectivity.
468
469 **Supporting Material**
470 Synthesis and characterization of thiols and characterization of nanoparticles. ESR experimental
471 details. XPS characterization of monolayer-protected nanoparticles. Additional results.
472
473 **Acknowledgements**
474 This research was supported by the Italian Ministry of University Research through the projects
475 PRIN2017 NiFTy (2017MYBTXC to L.P.), "Structure and function at the nanoparticle
476 biointerface" (RBSI14PBC6 to P.P.), (2017E44A9P to M. L.), by the University of Trieste (FRA
477 2018 to L.P.) and by the Jan Evangelista Purkyně University (grant No. UJEP-IGA-TC-2019-53-
478 02-2 to Z. P.). CERIC-ERIC consortium is acknowledged for the access to the Material Science
479 beamline at the Elettra synchrotron radiation facility (proposal number 20192081). Prof.
480 Alessandro Baraldi is kindly acknowledged for very helpful suggestions and discussion for XPS

measurements and data analysis. We thank Cristian Gabellini for instructive suggestions on data manipulation.

Author contribution

E.P. and M.Ş. made the synthesis/purification and the basic characterization of gold nanoparticles; M.Ş. contributed to the writing of the experimental part of synthesis and characterization; M.D. contributed to samples characterization and XPS measurements; P.Pengo contributed to the characterization of gold nanoparticles, supervised the synthetic work, partecipated to general discussion and contributed to the first draft of the manuscript; D.M. optimized the molecular models and carried out MD analysis; D.M. and Z.P. performed MD calculations; S.F. and L.B performed XPS data acquisition; L.B. supervised XPS experiments, elaborated XPS data, and contributed to the writing of the manuscript; P.F. contributed to ESR measurements; M.L. supervised ESR experiments, elaborated ESR data, participated to general discussion; P.Posocco supervised MD simulations and data analysis; L.P. and P.Posocco conceived the project; L.P. coordinated all contributions; L.P., P.Posocco and M.L. analyzed and discussed the results and contributed to writing the manuscript and prepared the final version.

Conflict of Interest

There are no conflicts to declare.

References

[1] J. R. Banavar, T. J. Cooke, A. Rinaldo, A. Maritan, *Proc. Natl. Acad. Sci.* **2014**, *111*, 3332.

[2] D. W. Sanders, N. Kedersha, D. S. W. Lee, A. R. Strom, V. Drake, J. A. Riback, D. Bracha, J. M. Eeftens, A. Iwanicki, A. Wang, M. T. Wei, G. Whitney, S. M. Lyons, P. Anderson, W. M. Jacobs, P. Ivanov, C. P. Brangwynne, *Cell* **2020**, *181*, 306.

[3] Z. Liu, X. Han, R. Chen, K. Zhang, Y. Li, S. Fruge, J. H. Jang, Y. Ma, L. Qin, *ACS Appl. Mater. Interfaces* **2017**, *9*, 22143.

[4] C. Luschnig, G. Vert, *Development* **2014**, *141*, 2924.

[5] J. Zhao, M. H. Stenzel, *Polym. Chem.* **2018**, *9*, 259.

[6] S. Shinoda, H. Tsukube, *Chem. Sci.* **2011**, *2*, 2301.

[7] M. L. Bender, E. T. Kaiser, *J. Am. Chem. Soc.* **1962**, *84*, 2556.

[8] Y. Murakami, J.-I. Kikuchi, Y. Hisaeda, O. Hayashida, *Chem. Rev.* **1996**, *96*, 721.

[9] C. A. Bunton, F. Nome, F. H. Quina, L. S. Romsted, *Acc. Chem. Res.* **1991**, *24*, 357.

[10] Y. Murakami, Y. Hisaeda, X.-M. Song, T. Ohno, *J. Chem. Soc., Perkin Trans. 2* **1992**, *9*, 1527.

[11] J. T. Groves, R. Neumann, *J. Am. Chem. Soc.* **1989**, *111*, 2900.

[12] J. T. Groves, S. B. Ungashe, *J. Am. Chem. Soc.* **1990**, *112*, 7796.

[13] R. Ueoka, Y. Matsumoto, R. A. Moss, S. Swarup, A. Sugii, K. Harada, J. Kikuchi, Y. Murakami, *J. Am. Chem. Soc.* **1988**, *110*, 1588.

[14] J. C. Love, L. A. Estroff, J. K. Kriebel, R. G. Nuzzo, G. M. Whitesides, *Chem. Rev.* **2005**, *105*, 1103.

[15] M. De, P. S. Ghosh, V. M. Rotello, *Adv. Mater.* **2008**, *20*, 4225.

[16] J. Czescik, S. Zamolo, T. Darbre, R. Rigo, C. Sissi, A. Pecina, L. Riccardi, M. De Vivo, F. Mancin, P. Scrimin, *Angew. Chem. Int. Ed.* **2021**, *60*, 1423.

[17] M. A. Boles, D. Ling, T. Hyeon, D. V. Talapin, *Nat. Mater.* **2016**, *15*, 141.

[18] N. D. Burrows, W. Lin, J. G. Hinman, J. M. Dennison, A. M. Vartanian, N. S. Abadeer, E. M. Grzincic, L. M. Jacob, J. Li, C. J. Murphy, *Langmuir* **2016**, *32*, 9905.

[19] M. Wu, A. M. Vartanian, G. Chong, A. K. Pandiakumar, R. J. Hamers, R. Hernandez, C. J. Murphy, *J. Am. Chem. Soc.* **2019**, *141*, 4316.

[20] F. P. Cometto, Z. Luo, S. Zhao, J. A. Olmos-Asar, M. M. Mariscal, Q. Ong, K. Kern, F. Stellacci, M. Lingenfelder, *Angew. Chem. Int. Ed.* **2017**, *56*, 16526.

[21] C. Weeraman, A. K. Yatawara, A. N. Bordenyuk, A. V. Benderskii, *J. Am. Chem. Soc.* **2006**, *128*, 14244.
[22] W. Edwards, N. Marro, G. Turner, E. R. Kay, *Chem. Sci.* **2018**, *9*, 125.
[23] P. U. Atukorale, Z. P. Guven, A. Bekdemir, R. P. Carney, R. C. Van Lehn, D. S. Yun, P. H. Jacob Silva, D. Demurtas, Y.-S. Yang, A. Alexander-Katz, F. Stellacci, D. J. Irvine, *Bioconj. Chem.* **2018**, *29*, 1131.
[24] S. Sabella, R. P. Carney, V. Brunetti, M. A. Malvindi, N. Al-Juffali, G. Vecchio, S. M. Janes, O. M. Bakr, R. Cingolani, F. Stellacci, P. P. Pompa, *Nanoscale* **2014**, *6*, 7052.
[25] D. Marson, F. Guida, M. Şologan, S. Boccardo, P. Pengo, F. Perissinotto, V. Iacuzzi, E. Pellizzoni, S. Polizzi, L. Casalis, L. Pasquato, S. Pacor, A. Tossi, P. Posocco, *Small* **2019**, *15*, 1900323.
[26] M. Şologan, C. Cantarutti, S. Bidoggia, S. Polizzi, P. Pengo, L. Pasquato, *Faraday Discuss.* **2016**, *191*, 527.
[27] A. Centrone, E. Penzo, M. Sharma, J. W. Myerson, A. M. Jackson, N. Marzari, F. Stellacci, *Proc. Natl. Acad. Sci.* **2008**, *105*, 9886.
[28] D. F. Moyano, Y. Liu, D. Peer, V. M. Rotello, *Small* **2016**, *12*, 76.
[29] P. Pengo, M. Şologan, L. Pasquato, F. Guida, S. Pacor, A. Tossi, F. Stellacci, D. Marson, S. Boccardo, S. Pricl, P. Posocco, *Eur. Biophys. J.* **2017**, *46*, 749.
[30] M. D. Manning, A. L. Kwansa, T. Oweida, J. S. Peerless, A. Singh, Y. G. Yingling, *Biointerphases* **2018**, *13*, 06D502.
[31] F. Muraca, L. Boselli, V. Castagnola, K. A. Dawson, *ACS Appl. Bio Mater.* **2020**, *3*, 3800.
[32] L. Boselli, E. Polo, V. Castagnola, K. A. Dawson, *Angew. Chem. Int. Ed.* **2017**, *56*, 4215.
[33] M. Siek, K. Kandere-Grzybowska, B. A. Grzybowski, *Acc. Mater. Res.* **2020**, *1*, 188.
[34] P. D. Jadzinsky, G. Calero, C. J. Ackerson, D. A. Bushnell, R. D. Kornberg, *Science* **2007**, *318*, 430.
[35] C. Zeng, Y. Chen, K. Kirschbaum, K. J. Lambright, R. Jin, *Science* **2016**, *354*, 1580.
[36] Y. Li, T. Higaki, X. Du, R. Jin, *Adv. Mater.* **2020**, *32*, 1905488.
[37] E. Colangelo, J. Comenge, D. Paramelle, M. Volk, Q. Chen, R. Lévy, *Bioconj. Chem.* **2017**, *28*, 11.
[38] P. K. Ghorai, S. C. Glotzer, *J. Phys. Chem. C* **2007**, *111*, 15857.
[39] D. S. Bolintineanu, J. M. D. Lane, G. S. Grest, *Langmuir* **2014**, *30*, 11075.

[40] A. K. Giri, E. Spohr, *J. Phys. Chem. C* **2018**, *122*, 26739.
[41] P. Posocco, C. Gentilini, S. Bidoggia, A. Pace, P. Franchi, M. Lucarini, M. Fermeglia, S. Pricl, L. Pasquato, *ACS Nano* **2012**, *6*, 7243.
[42] M. Şologan, D. Marson, S. Polizzi, P. Pengo, S. Boccardo, S. Pricl, P. Posocco, L. Pasquato, *ACS Nano* **2016**, *10*, 9316.
[43] Z. Luo, D. Marson, Q. K. Ong, A. Loiudice, J. Kohlbrecher, A. Radulescu, A. Krause-Heuer, T. Darwish, S. Balog, R. Buonsanti, D. I. Svergun, P. Posocco, F. Stellacci, *Nat. Commun.* **2018**, *9*, 1343.
[44] W. D. Luedtke, U. Landman, *J. Phys. Chem. B* **1998**, *102*, 6566.
[45] U. Landman, W. D. Luedtke, *Faraday Discuss.* **2004**, *125*, 1.
[46] A. Badia, W. Gao, S. Singh, L. Demers, L. Cuccia, L. Reven, *Langmuir* **1996**, *12*, 1262.
[47] H. Schmitt, A. Badia, L. Dickinson, L. Reven, R. B. Lennox, *Adv. Mater.* **1998**, *10*, 475.
[48] P. Fiurasek, L. Reven, *Langmuir* **2007**, *23*, 2857.
[49] M. Lucarini, P. Franchi, G. F. Pedulli, P. Pengo, P. Scrimin, L. Pasquato, *J. Am. Chem. Soc.* **2004**, *126*, 9326.
[50] E. Ertem, M. Diez-Castellnou, Q. K. Ong, F. Stellacci, *Chem. Rec*. **2018**, *18*, 819.
[51] B. Perrone, S. Springhetti, F. Ramadori, F. Rastrelli, F. Mancin, *J. Am. Chem. Soc.* **2013**, *135*, 11768.
[52] D. Marson, Z. Posel, P. Posocco, *Langmuir* **2020**, *36*, 5671.
[53] C. Pezzato, S. Maiti, J. L. Y. Chen, A. Cazzolaro, C. Gobbo, L. J. Prins, *Chem. Commun*. **2015**, *51*, 9922.
[54] C. K. Kim, P. Ghosh, C. Pagliuca, Z.-J. Zhu, S. Menichetti, V. M. Rotello, *J. Am. Chem. Soc.* **2009**, *131*, 1360.
[55] M. Boccalon, S. Bidoggia, F. Romano, L. Gualandi, P. Franchi, M. Lucarini, P. Pengo, L. Pasquato, *J. Mater. Chem. B* **2015**, *3*, 432.
[56] M. Lucarini, P. Franchi, G. F. Pedulli, C. Gentilini, S. Polizzi, P. Pengo, P. Scrimin, L. Pasquato, *J. Am. Chem. Soc.* **2005**, *127*, 16384.
[57] C. Gentilini, P. Franchi, E. Mileo, S. Polizzi, M. Lucarini, L. Pasquato, *Angew. Chem. Int. Ed.* **2009**, *48*, 3060.
[58] C. Gentilini, F. Evangelista, P. Rudolf, P. Franchi, M. Lucarini, L. Pasquato, *J. Am. Chem. Soc.* **2008**, *130*, 15678.

[59] S. Bidoggia, F. Milocco, S. Polizzi, P. Canton, A. Saccani, B. Sanavio, S. Krol, F. Stellacci, P. Pengo, L. Pasquato, *Bioconj. Chem.* **2017**, *28*, 43.
[60] T. R. Graham, R. Renslow, N. Govind, S. R. Saunders, *J. Phys. Chem. C* **2016**, *120*, 19837.
[61] J. Wang, R. M. Wolf, J. W. Caldwell, P. A. Kollman, D. A. Case, *J. Comput. Chem.* **2004**, *25*, 1157.
[62] J. Wang, W. Wang, P. A. Kollman, D. A. Case, *J. Mol. Graph. Model.* **2006**, *25*, 247.
[63] V. Barone, A. Bencini, M. Cossi, A. D. Matteo, M. Mattesini, F. Totti, *J. Am. Chem. Soc.* **1998**, *120*, 7069.
[64] R. Improta, A. di Matteo, V. Barone, *Theor. Chem. Acc.* **2000**, *104*, 273.
[65] E. Vanquelef, S. Simon, G. Marquant, E. Garcia, G. Klimerak, J. C. Delepine, P. Cieplak, F.-Y. Dupradeau, *Nucleic Acids Res.* **2011**, *39*, W511.
[66] H. Heinz, T.-J. Lin, R. Kishore Mishra, F. S. Emami, *Langmuir* **2013**, *29*, 1754.
[67] A. K. Chew, R. C. Van Lehn, *J. Phys. Chem. C* **2018**, *122*, 26288.
[68] D.A. Case, I.Y. Ben-Shalom, S.R. Brozell, D.S. Cerutti, I. T.E. Cheatham, V.W.D. Cruzeiro, T.A. Darden, R.E. Duke, D. Ghoreishi, M.K. Gilson, H. Gohlke, A.W. Goetz, D. Greene, R Harris, N. Homeyer, S. Izadi, A. Kovalenko, T. Kurtzman, T.S. Lee, S. LeGrand, P. Li, C. Lin, J. Liu, T. Luchko, R. Luo, D.J. Mermelstein, K.M. Merz, Y. Miao, G. Monard, C. Nguyen, H. Nguyen, I. Omelyan, A. Onufriev, F. Pan, R. Qi, D.R. Roe, A. Roitberg, C. Sagui, S. Schott-Verdugo, J. Shen, C.L. Simmerling, J. Smith, R. Salomon-Ferrer, J. Swails, R.C. Walker, J. Wang, H. Wei, R.M. Wolf, X. Wu, L. Xiao, D.M. York and P. A. Kollman, AMBER 2018, University of California, San Francisco.
[69] R. Salomon-Ferrer, D. A. Case, R. C. Walker, *Wiley Interdiscip. Rev. Comput. Mol. Sci.* **2013**, *3*, 198.
[70] R. Salomon-Ferrer, A. W. Götz, D. Poole, S. Le Grand, R. C. Walker, *J. Chem. Theory Comput.* **2013**, *9*, 3878.
[71] S. Le Grand, A. W. Götz, R. C. Walker, *Comput. Phys. Commun.* **2013**, *184*, 374.
[72] A. K. Boal, V. M. Rotello, *Langmuir* **2000**, *16*, 9527.
[73] L. Riccardi, L. Gabrielli, X. Sun, F. De Biasi, F. Rastrelli, F. Mancin, M. De Vivo, *Chem* **2017**, *3*, 92.

[74] X. Sun, L. Riccardi, F. De Biasi, F. Rastrelli, M. De Vivo, F. Mancin, *Angew. Chem. Int. Ed.* **2019**, *58*, 7702.

[75] A. G. Shard, *J. Phys. Chem. C* **2012**, *116*, 16806.

Graphical abstract